

A Model-Predictive Gust Load Alleviation Controller for a Highly Flexible Aircraft

Sohrab Haghighat ^{*}, Hugh H. T. Liu [†], Joaquim R. R. A. Martins [‡]

In this paper, a gust load alleviation system based on model-predictive control is developed for a very flexible aircraft. Two main contributions presented in this work are as follows. First, a unified dynamics framework is developed to represent the full six-degrees-of-freedom rigid body along with the structural dynamics. This allows for an integrated control design to account for maneuverability (flying qualities) and aeroelasticity simultaneously, leading to a new and improved configuration for a very flexible aircraft. Second, an improved model-predictive control formulation is proposed for stabilization and gust load alleviation. The performance of the model-predictive control is further improved by introducing an additional feedback loop to increase the prediction accuracy. To demonstrate the effectiveness of the proposed approach, the integrated formulation is compared with existing approaches. Further, the load alleviation performance is evaluated for various discrete and continuous gusts.

I. Introduction

Aircraft structures are required to sustain critical loading conditions during maneuvers or when flying through atmospheric turbulence. The use of active control has been extensively investigated, for example the alleviation of the dynamic load [1, 2, 3, 4, 5, 6] and the suppression of aeroelastic effects [7, 8]. The application of active-control techniques to large-aspect-ratio aircraft has recently become more prevalent [9]. Active structural control techniques can avoid catastrophic failure by preventing highly flexible aircraft wings from deforming to an unexpected shape, as happened in the Helios aircraft accident [10].

A wide range of aeroelastic models and control techniques have been considered for active aeroelastic control. In a seminal paper, Karpel [8] applied a static output feedback controller to a simple wing section to perform gust load alleviation (GLA) and flutter suppression. The feedback matrix coefficients were solved to move the closed-loop poles of the system to the desired locations.

Early efforts in aeroservoelasticity were based on flexible aircraft models consisting of rigid-body equations and a series of second-order differential equations representing the structural modes [11, 12]. McLean and Prasad [11] used a linear quadratic optimal controller to reduce the wing bending moment of the C-5A Galaxy aircraft. The simulation results showed that the application of the control system led to less oscillatory motion in the wing bending moment; this helps to reduce the accumulation of fatigue cycles in the aircraft wing. Aouf *et al.* [12] employed optimal and robust control methods to perform GLA on a flexible variant of the B-52 aircraft. The controller took advantage of ailerons and horizontal canards to reduce the transient peak value of the structural loadings caused by stochastic gust excitation. To obtain unsteady measurements and a reduced-order model, Silva *et al.* [13] performed experimental analysis on the SensorCraft wind-tunnel model at the NASA Langley transonic dynamics tunnel. The model was used to develop a simple GLA controller using the generalized predictive control method. Simulated open- and closed-loop results indicated that the controller had significantly lowered the gust response.

The application of adaptive feed-forward controllers for GLA has also been reported [14, 15, 16]. The main challenge for a feed-forward controller is the availability of a reliable gust-induced angle of attack measurement. Recently, Dillsaver *et al.* [17] designed a GLA controller for the highly flexible flying wing X-HALE [18]. A linear quadratic Gaussian (LQG) controller was designed and applied to the linear reduced-order model representing the aircraft dynamics. The controller was shown to reduce the peak wing curvatures by an average of 47% and the RMS curvatures by an average of 83.7%.

The performance of GLA systems also depends on the control surface effectiveness. Moulin and Karpel [2] investigated the effectiveness of different control surfaces in the GLA of a large transport aircraft. A baseline model

^{*}PhD Candidate, University of Toronto Institute for Aerospace Studies, 4925 Dufferin Street, Toronto, ON, Canada M3H 5T6, AIAA Student Member

[†]Associate Professor, University of Toronto Institute for Aerospace Studies, 4925 Dufferin Street, Toronto, ON, Canada M3H 5T6, AIAA Senior Member

[‡]Associate Professor, Department of Aerospace Engineering, University of Michigan, 1320 Beal Avenue, Ann Arbor, MI, AIAA Senior Member

with aileron control was compared with models equipped with an under-wing control surface and a wing-tip control surface. The three models were excited with a $(1 - \cos)$ discrete gust profile. It was shown that the new surfaces were more effective at relaxing the wing structure. Specifically, ailerons lose their effectiveness at higher speeds, whereas the other two control surfaces become even more effective.

We develop the nonlinear equations of motion for a highly flexible aircraft using Lagrange's equations for quasi-coordinates. The developed equations can effectively integrate large rigid-body motions with structural deflections. We use a three-dimensional panel method in combination with the eigensystem realization algorithm (ERA) to obtain a time-domain reduced-order model to represent the unsteady aerodynamics. To capture large, nonlinear structural deformations, we develop a co-rotational framework based on Euler–Bernoulli beam elements. We introduce a model-predictive control (MPC) framework to address GLA for very flexible aircraft. Predictive controllers are generally sensitive to the accuracy of the future output prediction, and their performance can be adversely affected by inaccurate predictions. We propose a technique to increase the prediction accuracy of the MPC, which improves the overall controller performance.

The novelty of this framework is twofold. First, we develop a unified dynamics framework to represent the full six-degrees-of-freedom rigid body along with the structural dynamics. This allows for an integrated control design to account for rigid-body and aeroelastic control simultaneously, leading to overall improvement for a very flexible aircraft. The derived formulations make it possible to realize the multidisciplinary synthesis of an actively controlled aeroservoelastic wing at the conceptual design phase. Secondly, we propose an improved MPC for stabilization and GLA. The introduction of prediction enhancement (PE) improves the performance of the controller in the presence of disturbance (gust) and model uncertainties.

We present a comparison study to highlight the significance of inertial interaction in flexible aircraft modeling. A Bode diagram clearly demonstrates that the exclusion of inertial interaction significantly affects the model accuracy at both low and high frequencies. To demonstrate the effectiveness of the proposed controller, we evaluate the performance of the system for an aircraft passing through various discrete and continuous gusts. The $(1 - \cos)$ profile is used to represent discrete gusts, and the Dryden gust model is used to generate continuous gust excitations. We compare our MPC with PE to the traditional MPC and the linear quadratic (LQ) control approach to show the superiority of our technique in structural load relaxation problems.

Section II of this paper discusses the aeroservoelastic formulation and the general nonlinear form of the equations for a deformable aircraft. Sections III and IV present the nonlinear structural modeling and the construction of the aerodynamic ROM. Section V describes the MPC formulation. Section VI discusses the numerical study, and Section VII provides concluding remarks.

II. Aeroservoelastic Formulation

Early efforts in aeroservoelasticity were based on flexible aircraft models consisting of traditional rigid-body equations and a series of second-order differential equations representing the structural modes [11, 12]. Recently, more detailed mathematical formulations of flexible aircraft flight dynamics have been developed. Schmidt and Raney developed the equations of motion for a flexible aircraft using the mean-axes method [19]. Some of their assumptions, including the application of aerodynamic strip theory and small structural deflections, make this approach less appropriate for modeling highly flexible aircraft. More rigorous formulations using a body-fixed axis system have also been developed [20, 21, 22, 23, 24, 25].

The development of a mathematical model that integrates flight dynamics with other disciplines, such as structures and aerodynamics, is the key to controlling a highly flexible aircraft. In this section, we derive the nonlinear equations of motion of a highly flexible aircraft using a body-fixed axis system. We begin with Lagrange's equations for quasi-coordinates,

$$\frac{d}{dt} \left(\frac{\partial L}{\partial \mathbf{V}_c} \right) + \omega^\times \frac{\partial L}{\partial \mathbf{V}_c} - C_{bi} \frac{\partial L}{\partial \mathbf{R}_c} = \mathbf{F}, \quad (1)$$

$$\frac{d}{dt} \left(\frac{\partial L}{\partial \boldsymbol{\omega}} \right) + V_c^\times \frac{\partial L}{\partial \mathbf{V}_c} + \omega^\times \frac{\partial L}{\partial \boldsymbol{\omega}} - D^{-T} \frac{\partial L}{\partial \boldsymbol{\theta}} = \mathbf{M}, \quad (2)$$

$$\frac{d}{dt} \left(\frac{\partial \hat{L}}{\partial \mathbf{v}} \right) - \frac{\partial \hat{T}}{\partial \mathbf{d}} + \frac{\partial \hat{\mathcal{F}}}{\partial \mathbf{v}} + \mathcal{L} \mathbf{d} = \hat{U}, \quad (3)$$

where L and T are the Lagrangian and kinetic energy, respectively, of the system. Vectors \mathbf{F} and \mathbf{M} are the total forces

and moments acting on the rigid body. \mathcal{F} represents Rayleigh's dissipation term, U represents the distributed forces acting on the aircraft structure, (\cdot) indicates the volume density of the energy terms, and $(\cdot)^\times$ is the cross-product operator representing a skew-symmetric matrix with the following form:

$$\boldsymbol{\omega} = \{\omega_1 \quad \omega_2 \quad \omega_3\}^T \Rightarrow \boldsymbol{\omega}^\times = \begin{bmatrix} 0 & -\omega_3 & \omega_2 \\ \omega_3 & 0 & -\omega_1 \\ -\omega_2 & \omega_1 & 0 \end{bmatrix}. \quad (4)$$

The two transformation matrices, C_{bi} and D , transform the inertial translational velocities and the inertial rotational velocities, respectively, into the corresponding velocity vectors in the body-fixed coordinate system. Figure 1 shows a deformable aircraft with the original wing and its deformation, as well as the associated axis systems. \mathbf{F}_I represents the inertial frame and \mathbf{F}_B the body-fixed frame, not necessarily connected to the center of mass. The absolute position and velocity of an infinitesimal mass element dm on the aircraft are given by

$$\begin{aligned} \mathbf{R} &= \mathbf{R}_c + \mathbf{r} + \mathbf{d}, \\ \mathbf{V} &= \dot{\mathbf{R}} = \mathbf{V}_c + \boldsymbol{\omega} \times (\mathbf{r} + \mathbf{d}) + \mathbf{v}. \end{aligned} \quad (5)$$

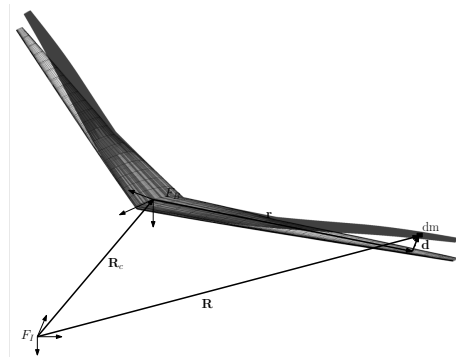


Figure 1. Schematic drawing of deformed aircraft and position vectors

Figure 1 shows the location vector of the body-axis \mathbf{R}_c , the mass-element rigid distribution vector \mathbf{r} , and the displacement of the mass element \mathbf{d} . The deformational velocity of the mass element is represented by \mathbf{v} . Finally, \mathbf{V}_c is the translational velocity of the body-frame origin, and $\boldsymbol{\omega}$ is the rotational velocity of the body-frame \mathbf{F}_B . The structural deformations can be expressed in a discrete finite-element formulation or as a linear combination of the mode shapes. A common choice for these mode shapes is the eigenvectors of the structural system. Although the modal representation is often applied in dynamic response and stability analysis, static aeroelastic analysis is usually based on discrete finite-element methods. This is because the modal representation does not adequately capture the effect of concentrated forces, such as the weight of external stores, unless the structural modes are calculated using large fictitious masses at the locations of the lumped forces [26]. In our case, no lumped forces are present on the aircraft wing, and so we use the modal representation for both the static and dynamic analysis. The structural displacement and velocity can be expressed in the modal form as follows:

$$\mathbf{d} = \boldsymbol{\phi}_r \boldsymbol{\xi} \Rightarrow \mathbf{v} = \boldsymbol{\phi}_r \boldsymbol{\eta}, \quad (6)$$

where $\boldsymbol{\xi}$ is a vector of modal amplitudes, $\boldsymbol{\eta}$ is the rate of change of the modal amplitudes, and $\boldsymbol{\phi}_r$ represents the modal deflection at location \mathbf{r} . This modal deflection matrix has the following form:

$$\boldsymbol{\phi}_r = \begin{bmatrix} x_{r,1} & x_{r,2} & \cdots & x_{r,n} \\ y_{r,1} & y_{r,2} & \cdots & y_{r,n} \\ z_{r,1} & z_{r,2} & \cdots & z_{r,n} \end{bmatrix}, \quad (7)$$

where $x_{r,i}$ is the deformation at location \mathbf{r} in the x direction due to the i^{th} structural shape function. Note that the adoption of the modal representation for structural deformations does not impose any restrictions on the modeling of large nonlinear structural deformations. In Section III we briefly discuss the computation of nonlinear structural deformations using a co-rotational framework.

The gravitational force is modeled as a distributed force, and therefore the following terms in Eqs. (1) and (2) vanish:

$$\frac{\partial L}{\partial \mathbf{R}_c} = 0, \quad \frac{\partial L}{\partial \boldsymbol{\theta}} = 0. \quad (8)$$

Using the structural shape functions, we can adapt Eq. (3) to the modal form as follows:

$$\frac{d}{dt} \left(\frac{\partial L}{\partial \boldsymbol{\eta}} \right) - \frac{\partial T}{\partial \boldsymbol{\xi}} + \frac{\partial \mathcal{U}}{\partial \boldsymbol{\xi}} + \frac{\partial \mathcal{F}}{\partial \boldsymbol{\eta}} = \mathbf{f}_e, \quad (9)$$

where \mathcal{U} and \mathcal{F} represent the strain energy and Rayleigh's dissipation for the complete aircraft structure. Also, \mathbf{f}_e denotes the generalized modal forces that act on the aircraft structure.

A. Kinetic Energy

The kinetic energy of a deformable aircraft can be formulated as follows:

$$\begin{aligned} T = & \frac{1}{2} \int_v \rho \mathbf{V}^T \mathbf{V} dv = \frac{1}{2} m \mathbf{V}_c^T \mathbf{V}_c + \mathbf{V}_c^T \left[\int_v \rho \left(r^\times + (\phi_r \boldsymbol{\xi})^\times \right)^T dv \right] \boldsymbol{\omega} + \mathbf{V}_c^T \left[\int_v \rho \phi_r dv \right] \boldsymbol{\eta} \\ & + \boldsymbol{\omega}^T \left[\int_v \rho \left(r^\times + (\phi_r \boldsymbol{\xi})^\times \right) \phi_r dv \right] \boldsymbol{\eta} + \frac{1}{2} \boldsymbol{\omega}^T \underbrace{\left[\int_v \rho \left(r^\times + (\phi_r \boldsymbol{\xi})^\times \right) \left(r^\times + (\phi_r \boldsymbol{\xi})^\times \right)^T dv \right]}_J \boldsymbol{\omega} \\ & + \frac{1}{2} \boldsymbol{\eta}^T \underbrace{\left[\int_v \rho \phi_r^T \phi_r dv \right]}_{M_{ee}} \boldsymbol{\eta}. \end{aligned} \quad (10)$$

In the above equation, J represents the aircraft moment of inertia matrix and M_{ee} is the aircraft structure modal mass matrix. If the origin of \mathbf{F}_B is placed at the undeformed aircraft center of gravity, the term $\int_v \rho r^\times dv$ is zero.

B. Potential Energy

The strain energy of an elastic system can be written

$$\mathcal{U} = \frac{1}{2} \boldsymbol{\xi}^T \Phi^T K \Phi \boldsymbol{\xi} = \frac{1}{2} \boldsymbol{\xi}^T K_{ee} \boldsymbol{\xi}, \quad (11)$$

where K_{ee} is the aircraft structure modal stiffness matrix, and Φ is the matrix of the shape functions for all nodes on the aircraft, i.e., $\Phi^T = [\phi_{\mathbf{r}_1}^T \quad \phi_{\mathbf{r}_2}^T \quad \cdots \quad \phi_{\mathbf{r}_m}^T]^T$.

C. Nonlinear Equations of Motion

If we substitute the kinetic and potential energy into Eqs. (1), (2), and (9) and rearrange them, the equations of motion of a deformable aircraft become

$$\begin{aligned} \begin{bmatrix} m\mathcal{I}_{3 \times 3} & X_1^T & S_1 \\ X_1 & J & S_2 + X_2 \\ S_1^T & S_2^T + X_2^T & M_{ee} \end{bmatrix} \begin{Bmatrix} \dot{\mathbf{V}}_c \\ \dot{\boldsymbol{\omega}} \\ \dot{\boldsymbol{\eta}} \end{Bmatrix} = \\ - \begin{bmatrix} m\omega^\times & \omega^\times X_1^T & 2\omega^\times S_1 \\ \omega^\times X_1 & \omega^\times J + \dot{J} + V_c^\times X_1^T & \omega^\times (S_2 + X_2) \\ -S_1^T \omega^\times T & \int_v \rho \phi_r^T \omega^\times r^\times T dv & 2 \int_v \rho \phi_r^T \omega^\times \phi_r dv + C_{ee} \end{bmatrix} \begin{Bmatrix} \mathbf{V}_c \\ \boldsymbol{\omega} \\ \boldsymbol{\eta} \end{Bmatrix} \\ - \begin{bmatrix} \mathcal{O}_{6 \times 6} & \mathcal{O}_{6 \times n} \\ \mathcal{O}_{n \times 6} & \int_v \rho \phi_r^T \omega^\times \phi_r dv + K_{ee} \end{bmatrix} \begin{Bmatrix} \mathbf{R}_c \\ \boldsymbol{\theta} \\ \boldsymbol{\xi} \end{Bmatrix} + \begin{bmatrix} mC_{bi} \\ X_1^T C_{bi} \\ S_1^T C_{bi} \end{bmatrix} \{\mathbf{g}\} + \begin{bmatrix} \mathbf{F} \\ \mathbf{M} \\ \mathbf{f}_e \end{bmatrix}. \end{aligned} \quad (12)$$

As mentioned before, \mathbf{F} and \mathbf{M} are the total forces and moments about the origin of the body-frame, including the propulsive and aerodynamic forces. The matrix C_{ee} represents the modal damping of the aircraft structure, and \mathbf{g} is the vector of gravitational acceleration. The generalized modal force \mathbf{f}_e acting on the aircraft structure is calculated as

$$\mathbf{f}_e = \int_s \phi_r^T p \hat{\mathbf{n}} ds, \quad (13)$$

where p is the pressure acting on the surface of the aircraft and $\hat{\mathbf{n}}$ is the surface normal vector. Matrices S_1 , S_2 , X_1 , and X_2 are the rigid-elastic interaction terms and are defined as follows:

$$\begin{aligned} S_1 &= \int_v \rho \phi_{\mathbf{r}} dv, \\ S_2 &= \int_v \rho r^{\times} \phi_{\mathbf{r}} dv, \\ X_1 &= \int_v \rho (\phi_{\mathbf{r}} \boldsymbol{\xi})^{\times} dv, \\ X_2 &= \int_v \rho (\phi_{\mathbf{r}} \boldsymbol{\xi})^{\times} \phi_{\mathbf{r}} dv, \\ \dot{J} &= \int_v \rho \left[(\phi_{\mathbf{r}} \boldsymbol{\eta})^{\times} \left(r^{\times} + (\phi_{\mathbf{r}} \boldsymbol{\xi})^{\times} \right)^T + \left(r^{\times} + (\phi_{\mathbf{r}} \boldsymbol{\xi})^{\times} \right) (\phi_{\mathbf{r}} \boldsymbol{\eta})^{\times T} \right] dv. \end{aligned} \quad (14)$$

Note that the integrals in Eq. (14) are all volumetric integrals whereas the integral in Eq. (13) is a surface integral. As an aircraft becomes more flexible, the relative magnitudes of the X_1 , X_2 , and \dot{J} terms with respect to the other terms in Eq. (12) become larger, which results in a stronger interaction between the two types of dynamics.

III. Structural Modeling

In aeroelastic modeling, beam elements have traditionally been used to represent the wing structure. The recently studied high altitude long endurance (HALE) planes have very flexible wing structures that deform beyond the limits that can be correctly captured by simple linear finite-element representations. In this work, we use linear three-dimensional Euler–Bernoulli beam elements in a co-rotational framework to model very large wing deformations. In a co-rotational formulation, the rigid-body motions are separated from the strain-producing deformations at the local element level. This is accomplished by attaching a local element reference frame to each element; this rotates and translates with the beam element. A more detailed description can be found in the nonlinear finite-element literature [27, 28, 29].

IV. Aerodynamic Modeling

We use a three-dimensional unsteady aerodynamic panel code to obtain the aerodynamic loads. The lifting surfaces are discretized using source and doublet panels, and the wake elements are represented by doublet panels. We compute the strength of the panels by enforcing the tangential flow condition at each panel. Using the pressure at each panel, we can compute the rigid-body forces and moments and the elastic generalized aerodynamic forces (GAFs). The efficient and accurate calculation of GAFs has always been a major challenge in aeroservoelastic analysis and optimization. Reduced-order models (ROMs) based on the Volterra theory of nonlinear systems have received significant attention as a way to overcome this challenge. The Volterra theory was first used to model unsteady aerodynamic systems by Silva [30] and has been developed further by other researchers [31, 32, 33, 34]. Volterra-based ROMs are based on the creation of linearized and nonlinear unsteady aerodynamic impulse/step responses that are then used in the Volterra series to provide the linearized and nonlinear responses of the system to arbitrary inputs. We can combine this method with a system identification technique such as the ERA [35] to construct state-space matrices (A_{aero} , B_{aero} , and C_{aero}) that represent the generalized aerodynamic forces. For more detailed information on the application of the Volterra theory and the ERA to unsteady aerodynamic modeling see [34].

We compute the pulse responses for each mode of an aeroelastic system using the developed 3D panel code. As reported by Raveh and Mavris [32], the inclusion of the second-order kernel terms does not significantly improve the accuracy of the results. Therefore, we use only a first-order kernel (the obtained pulse responses), and the Volterra theory is not applied to compute higher-order kernels. The recorded pulse responses, obtained from the excitations of the panel code, are the Markov parameters ($Y_k = C_{\text{aero}} A_{\text{aero}}^{k-1} B_{\text{aero}}$) that the ERA technique uses to reconstruct the state matrices.

V. Control System Design for GLA

A. Linearized State-Space Representation

To obtain a linear plant representation, needed to design a linear control system, we first linearize the equations of motion. In Eq. (12), terms such as X_1 , X_2 , and J are dependent on the structural deformation. Therefore, the aeroelastic analysis and the control system design should be based on the actual trimmed shape of the aircraft. As shown by Haghighat *et al.* [36], the design of a control system based on an undeformed linearized model can lead to instabilities. For straight rectilinear flight we can perform the linearization by substituting the perturbed flight parameters into Eq. (12) and ignoring the higher-order terms. For more general cases, the linearization process is not

tractable and therefore must be performed numerically. The linearized equations of motion for a straight level flight are

$$\begin{Bmatrix} \delta \dot{\mathbf{V}}_c \\ \delta \dot{\boldsymbol{\omega}} \\ \delta \dot{\boldsymbol{\eta}} \end{Bmatrix} = M^{-1} \left(\begin{bmatrix} \mathcal{O}_{3 \times 3} & m \widetilde{V}_{c_0} & \mathcal{O}_{3 \times n} \\ \mathcal{O}_{3 \times 3} & X_{1_0}^T V_{c_0} - \widetilde{V}_{c_0} X_{1_0} & \mathcal{O}_{3 \times n} \\ \mathcal{O}_{3 \times 3} & S_1^T V_{c_0} & -C_{ee} \end{bmatrix} \begin{Bmatrix} \delta \mathbf{V}_c \\ \delta \boldsymbol{\omega} \\ \delta \boldsymbol{\eta} \end{Bmatrix} \right. \\ \left. + \begin{bmatrix} \mathcal{O}_{3 \times 3} & mG & \mathcal{O}_{3 \times n} \\ \mathcal{O}_{3 \times 3} & X_{1_0} G & \mathcal{O}_{3 \times n} \\ \mathcal{O}_{3 \times 3} & S_1^T G & -K_{ee} \end{bmatrix} \begin{Bmatrix} \delta \mathbf{R}_c \\ \delta \boldsymbol{\theta} \\ \delta \boldsymbol{\xi} \end{Bmatrix} + \begin{Bmatrix} \delta \mathbf{F} \\ \delta \mathbf{M} \\ \delta \mathbf{f}_e \end{Bmatrix} \right), \quad (15)$$

where the M and G matrices are

$$M = \begin{bmatrix} m & X_{1_0}^T & S_1 \\ X_{1_0}^T & J_0 & S_2 + X_{2_0} \\ S_1^T & S_2^T + X_{2_0}^T & M_{ee} \end{bmatrix}, \quad G = \begin{bmatrix} 0 & -g \cos(\theta_0) & 0 \\ -g \cos(\theta_0) & 0 & 0 \\ 0 & g \sin(\theta_0) & 0 \end{bmatrix}. \quad (16)$$

The linearized inertia matrix (M) has off-diagonal terms that include the coupling between the two dynamics. Note that S_1 and S_2 are constant whereas X_{1_0} and X_{2_0} are shape-dependent and must be computed based on the trimmed shape of the aircraft. These equations are driven by the perturbed aerodynamic forces and moments, which can be represented using the ROM obtained for the aerodynamic forces and moments. Elevator and aileron deflections are the two major control inputs used here. The left and the right aileron deflect differentially for roll control, but they can also be controlled independently to perform load alleviation for the left or the right wing. The total control surface deflection for each aileron is calculated by adding these two components. Eq. (15), when augmented with the obtained aerodynamic ROM, can be expressed in a state-space form. The state vector and other system matrices are

$$\begin{cases} \mathbf{x}_{ac}^T = \{ \mathbf{V}_c & \boldsymbol{\omega} & \boldsymbol{\xi} & \boldsymbol{\eta} & \boldsymbol{\theta} & \mathbf{R}_c & \mathbf{x}_{aero} \} \\ \dot{\mathbf{x}}_{ac} = A \mathbf{x}_{ac} + B \mathbf{u} + B_g \mathbf{u}_g \\ \mathbf{y} = C \mathbf{x}_{ac} \end{cases}, \quad (17)$$

where $\boldsymbol{\theta}$ is the vector of Euler angles ($[\phi \ \theta \ \psi]^T$), and \mathbf{x}_{aero} is the state vector from the aerodynamic reduced-order model. The B_g matrix is used to model the effect of disturbances, such as gusts, on the aircraft dynamics. The stress levels are calculated based on the modal deflections as follows:

$$\sigma = SU\Phi\xi \quad (18)$$

where SU is a constant matrix that relates the von Mises stress to the nodal displacement; it can be formed when the structural mesh is generated. As is clear from the above equation, the stress level in the wing is directly proportional to the amplitude of the structural modes (ξ). Therefore, by ensuring that the modal amplitudes are close to zero we can maintain the stress at the steady-state level. The state-space representation is used to design a control system that performs rigid-body tracking and minimizes the structural deformations in order to lower the stress at the critical flight conditions. In this work, we consider only the longitudinal dynamics of the aircraft, and therefore the ailerons are applied symmetrically.

B. Gust Profile

As mentioned before, we use both discrete and continuous gust profiles. For discrete gust evaluation, we use a (1 - cos) gust profile of the following form:

$$w_g = \frac{\bar{w}_g}{2} \left(1 - \cos \frac{2\pi t}{L_g} \right), \quad (19)$$

where w_g is the vertical gust velocity, \bar{w}_g is the gust amplitude, and L_g is the gust length, nondimensionalized with respect to the time for a point in the aircraft to travel across the gust field. For continuous gust modeling, we use the Dryden model to create stochastic gust excitations. In this approach, the gust is modeled as a stationary, random Gaussian process with the prescribed power spectral density. For a continuous gust where the gust vector is generated using the Dryden gust model, we use a gust filter to generate the numerical values of the gust [37]:

$$G_w(s) = \bar{w}_g \sqrt{\frac{L}{\pi V}} \frac{1 + \frac{\sqrt{3}L}{V}s}{(1 + \frac{L}{V}s)^2}, \quad G_q(s) = \frac{\frac{s}{V}}{(1 + (\frac{4b}{\pi V})s)} G_w(s) \quad (20)$$

where $G_w(s)$ and $G_q(s)$ are the gust filters representing the vertical and rotational gust velocities. The parameter L represents the gust scale and V represents the aircraft flying speed. In this work, we set \bar{w}_g to 5 m/s for both the continuous and discrete cases.

C. Challenges

In aircraft control design, traditionally the rigid-body tracking is performed separately from the structural control, and the interaction of the structural and rigid-body dynamics is avoided by the introduction of notch filters. Because of the high flexibility of aircraft wings, there is a strong interaction between the rigid-body dynamics and the structural dynamics; this makes the design of a control system challenging. We must design a unified controller that considers both the rigid-body motion and the aircraft flexibility. Furthermore, the high flexibility of the aircraft structure results in a time delay between the control input deflections and the rigid-body motion of the aircraft. This delay results in a non-minimum phase system that is challenging to control. Finally, in a very flexible aircraft, the high-frequency structural modes are very lightly damped. This makes the design of a state observer challenging, because the transient response of the filter can adversely affect the closed-loop stability and performance. The first and second challenges above are addressed in the next section. However, the selection of appropriate sensors and the design of an observer filter are not addressed in this paper.

D. Model-Predictive Control

Model-predictive control (MPC), also known as receding horizon control (RHC), is a discrete method that is well known in optimal control [38]. Using this technique, we calculate the control signal by performing a constrained optimization over a finite control horizon (and in some cases a constraint horizon), indicated by the number of future control steps N_u at each sampling time. The increased capability of computer hardware and the advent of fast and reliable quadratic programming techniques have made it possible to apply MPC to problems with fast dynamics, such as path planning and aircraft dynamics [39, 40]. MPC is advantageous when a plant is nonlinear or time-varying and also when the states or inputs must be constrained [38, 41]. To address the model nonlinearities and the time-varying behavior arising in a maneuvering flight, we can perform successive linearization at each sampling time. Because GLA and rigid-body regulation are the main focus of this work, successive linearization is not performed, and we use the linearized model about the steady trimmed shape for the control design.

Since MPC is a discrete control method, we must use the discretized state-space representation of the plant. The desired performance is achieved by minimizing the following quadratic performance function below.

$$V(\mathbf{x}_k, \mathbf{U}, N_u, N_p) = \sum_{i=1}^{N_p-1} \left((\mathbf{x}_{k+i} - \mathbf{x}_{\text{ref},k+i})^T Q (\mathbf{x}_{k+i} - \mathbf{x}_{\text{ref},k+i}) \right) + \sum_{i=0}^{N_u-1} (\mathbf{u}_{k+i}^T R \mathbf{u}_{k+i}) + (\mathbf{x}_{k+N_p} - \mathbf{x}_{\text{ref},k+N_p})^T Q_f (\mathbf{x}_{k+N_p} - \mathbf{x}_{\text{ref},k+N_p}), \quad (21)$$

where \mathbf{x}_k , $\mathbf{x}_{\text{ref},k}$, and \mathbf{u}_k are the state, the reference state, and the control input vectors, respectively, at time-step k . The vector \mathbf{U} is the control signal sequence over the control horizon N_u . The variable N_p represents the prediction horizon, which can be longer than the control horizon. The matrices Q and R are the state and input weighting matrices, respectively. Finally, Q_f is the terminal weighting matrix. The predicted state sequence \mathbf{X} can be expressed, in a compact form, as a function of the future input sequence \mathbf{U} and the current state \mathbf{x}_k , i.e.,

$$\mathbf{X} = H\mathbf{U} + G\mathbf{x}_k, \text{ where } H = \begin{bmatrix} C_d B_d & & & \\ C_d A_d B_d & C_d B_d & & \\ \vdots & & \ddots & \\ C_d A_d^{N_u-1} B_d & C_d A_d^{N_u-2} B_d & \dots & C_d B_d \\ C_d A_d^{N_u} B_d & C_d A_d^{N_u-1} B_d & \dots & C_d A_d B_d \\ \vdots & & \ddots & \vdots \\ C_d A_d^{N_p-1} B_d & C_d A_d^{N_p-2} B_d & \dots & \sum_{i=0}^{N_p-N_u} C_d A_d^i B_d \end{bmatrix}, \quad G = \begin{bmatrix} A_d \\ A_d^2 \\ \vdots \\ A_d^{N_p} \end{bmatrix} \quad (22)$$

where $H\mathbf{U}$ represents the forced output, and $G\mathbf{x}_k$ is the free output due to the initial condition \mathbf{x}_k . In the absence of complete state information, the estimated values of the current state ($\hat{\mathbf{x}}_k$) must be used. In this work, as explained in Section C, we assume that the exact values of the current state vector are available for feedback. To avoid unrealistic control actions, we consider saturation of the control surface deflections and their rates. Therefore, the optimization problem becomes a constrained optimization problem, i.e.,

$$\begin{aligned} \min \quad & V(\mathbf{x}_k, \mathbf{U}, N_u, N_p) \\ \text{w.r.t.} \quad & \mathbf{U}, \\ \text{s.t.} \quad & \mathbf{u}_{\min} \leq \mathbf{u}_i \leq \mathbf{u}_{\max}, \\ & \Delta \mathbf{u}_{\min} \leq \Delta \mathbf{u}_i \leq \Delta \mathbf{u}_{\max}. \end{aligned} \quad (23)$$

The above constraints can also be expressed in a compact form as $F\mathbf{U} \leq \mathbf{c}$ where the matrix F and the vector \mathbf{c} are formed as follows:

$$F = \begin{bmatrix} \mathcal{I}_{N_u \cdot m} \\ -\mathcal{I}_{N_u \cdot m} \\ M \\ -M \end{bmatrix}, \quad \mathbf{c} = \begin{bmatrix} \mathbf{U}_{\max} \\ -\mathbf{U}_{\min} \\ \Delta\mathbf{U}_{\max} + \mathbf{b} \\ -\Delta\mathbf{U}_{\max} - \mathbf{b} \end{bmatrix}, \quad \text{with } M = \begin{bmatrix} \mathcal{I} & & & \\ -\mathcal{I} & \mathcal{I} & & \\ & & \ddots & \ddots \\ & & & -\mathcal{I} & \mathcal{I} \end{bmatrix}, \quad \text{and } \mathbf{b} = \begin{bmatrix} \mathbf{u}_{k-1} \\ 0 \\ \vdots \end{bmatrix}. \quad (24)$$

Using the compact formulation for the future output prediction and the constraints, we can write the problem as follows:

$$\begin{aligned} \min \quad & V(\hat{\mathbf{x}}_k, \mathbf{U}, N_u, N_p) = \mathbf{U}^T (H^T \hat{Q} H + \hat{R}) \mathbf{U} + 2(\hat{\mathbf{x}}_k^T G^T - \mathbf{X}_{\text{ref}}^T) \hat{Q} H \mathbf{U}, \\ \text{w.r.t.} \quad & \mathbf{U}, \\ \text{s.t.} \quad & F \cdot \mathbf{U} \leq \mathbf{c}, \end{aligned} \quad (25)$$

where \mathbf{X}_{ref} is the reference state sequence over the prediction horizon. Since GLA is the goal of this work, the reference input is constant over time. The matrices \hat{Q} and \hat{R} are block diagonal and can be written

$$\hat{Q} = \text{diag}[Q \quad Q \quad \cdots \quad Q_f], \quad \hat{R} = \text{diag}[R \quad R \quad \cdots \quad R]. \quad (26)$$

The above problem is a quadratic programming (QP) problem. For a positive definite weighting matrix Q , we can show that $H^T \hat{Q} H$ is also positive definite, and the optimization problem becomes a convex quadratic programming (CQP) problem for which the solution for the future input sequence \mathbf{U} is unique. Such problems can be solved efficiently using fast cone programming algorithms [42]. Figure 2 shows a schematic representation of the control system.

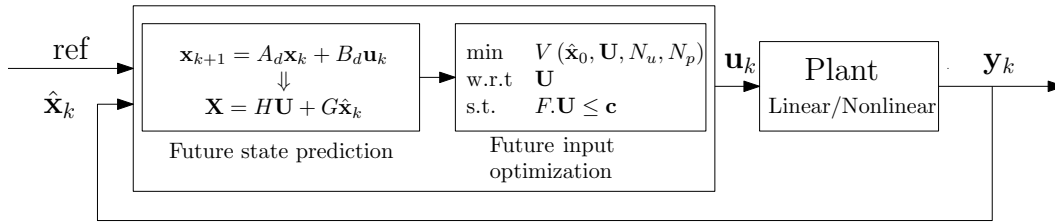


Figure 2. Block diagram of model-predictive control system

1. Stability of Model-Predictive Controller

It is well known that if a system is stabilizable and detectable, then a standard linear quadratic infinite-horizon optimal control problem yields an optimal stabilizing controller [43]. However, a linear finite-horizon model-predictive controller with a quadratic performance index is not asymptotically stabilizing in general. The use of a finite horizon, which is required to make the numerical optimization tractable, may destabilize the closed-loop system. The stability of finite-horizon MPC problems has been extensively studied, and techniques to ensure the stability of these systems have been developed [41, 38, 44]. It can be shown that an LQ model-predictive controller is stable *if and only if* the pair (A, B) is stabilizable, the pair $(A, Q^{1/2})$ is observable, and the cost monotonicity condition, $V(\mathbf{x}_k, \mathbf{U}^*, N+1) \leq V(\mathbf{x}_k, \mathbf{U}^*, N)$, is satisfied.

The cost monotonicity of a constrained MPC is guaranteed if any of the following terminal conditions is applied: (1) terminal equality constraints, (2) terminal set constraints, and (3) terminal penalty function. The first two approaches are restrictive, and in particular the terminal equality constraint may reduce the feasibility region. Richards and How [45] developed an analytical method for the performance prediction of a constrained MPC. They use a terminal inequality constraint along with a recursive tightening scheme that guarantees the stability of the system in the presence of disturbance. The application of the recursive terminal-constraint tightening allows the control designer to choose an initially wide terminal constraint, which improves the feasibility of the design. We use the terminal penalty approach. The cost monotonicity condition can be guaranteed under the application of terminal weighting if the terminal penalty function satisfies the following condition:

$$Q_f \geq Q + K^T R K + (A_d - B_d K)^T Q_f (A_d - B_d K) \quad (27)$$

for some $K \in \mathbf{R}^{m \times n}$.

For the proof of the above theorem see [38]. We choose the K matrix as the gain of an LQR controller with the same Q and R weighting matrices.

2. Model-Predictive Controller with PE

The performance of a model-predictive controller is highly dependent on its ability to predict the future state values. Poor state prediction may result in performance degradation and system instability. The discrepancies between the predicted values and the actual state values stem from unmodeled dynamics, system nonlinearities, parameter mismatches, and disturbances. We propose the addition of a feedback loop to the traditional formulation to improve the prediction accuracy of the predictive controller. We update the prediction at each sampling time, based on the difference between the previous step prediction and the estimated value of the state vector, as follows:

$$\begin{aligned} \mathbf{x}_{k+1}^p &= A_d \hat{\mathbf{x}}_k + B_d \mathbf{u}_k + L \underbrace{(\hat{\mathbf{x}}_k - \mathbf{x}_k^p)}_{\mathbf{e}_k}, \\ \mathbf{x}_{k+2}^p &= A_d^2 \hat{\mathbf{x}}_k + A_d B_d \mathbf{u}_k + B_d \mathbf{u}_{k+1} + L \mathbf{e}_k, \\ &\vdots \end{aligned} \quad (28)$$

where L is a transition matrix that represents the effect of the previous step error \mathbf{e}_k on the future output prediction. The above series of equations can be expressed in the following compact form:

$$\mathbf{X}^p = H\mathbf{U} + G\hat{\mathbf{x}}_k + G_o L \mathbf{e}_k, \quad \text{where } G_o = \begin{bmatrix} \mathcal{I} \\ A_d \\ A_d^2 \\ \vdots \end{bmatrix}. \quad (29)$$

With this equation for predicting the future states, the cost function becomes

$$V(\hat{\mathbf{x}}_k, \mathbf{U}, N_u, N_p) = \mathbf{U}^T \left(H^T \hat{Q} H + \hat{R} \right) \mathbf{U} + 2 \left(\hat{\mathbf{x}}_k^T G^T + \mathbf{e}_k^T L^T G_o^T - \mathbf{X}_{\text{ref}} \right) \hat{Q} H \mathbf{U}. \quad (30)$$

If L is set to zero, then the cost function is the same as the cost function in the traditional formulation. In the absence of detailed information about the disturbance and the unmodeled dynamics, an identity matrix of the appropriate size can be used for L . If the variation of the plant matrices from the nominal values is known, a better transition matrix can be constructed using the available information. Figure 3 shows this model-predictive controller with PE. A similar approach was used by Richards and How [46] to improve performance and guarantee controller stability in the absence of perfect measurement. They use the estimation error to modify the prediction performance to improve the closed-loop stability and performance. We assume the availability of perfect state information, and we use the proposed approach to improve the performance of the controller when stabilizing a damaged aircraft.

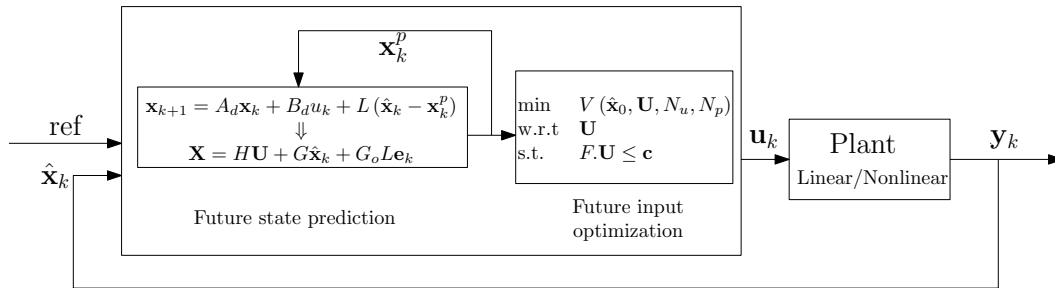


Figure 3. Block diagram of model-predictive control system

3. Model-Predictive Controller Applied to Non-Minimum Phase System

One of the difficulties in controlling a non-minimum phase system is the internal instability problem. This problem arises when the desired high performance level forces the controller to contain an implicit approximate inverse of the

system model. When the controller dynamics contains the inverse of a system model with unstable zeros, the cancellation of unstable poles and zeros causes internal instability. Garcia–Gabin *et al.* [47] showed how the application of a multivariable model-predictive controller to a non-minimum phase plant can lead to internal instabilities. It can be shown that if no control and state constraints are considered, the optimal control sequence can be calculated as follows:

$$\mathbf{U}^* = \left(H^T \hat{Q} H + \hat{R} \right)^{-1} H^T \hat{Q} (G \hat{\mathbf{x}}_k - \mathbf{X}_{\text{ref}}). \quad (31)$$

If the control effort is not penalized ($R = \mathcal{O}$) and the prediction and control horizons are equal (H is a square matrix) then the optimal control sequence becomes

$$\mathbf{U}^* = H^{-1} (G \hat{\mathbf{x}}_k - \mathbf{X}_{\text{ref}}). \quad (32)$$

If we substitute the optimal control sequence into Eq. (22), there is a cancellation of the unstable poles with unstable zeros that causes the internal instability. Penalizing the control effort and using a prediction horizon longer than the control horizon (tall H matrix) have been reported to avoid the internal instability [48]. We use control penalization to avoid internal instabilities.

VI. Numerical Results

We now apply our controller to a very flexible UAV undergoing discrete and continuous gusts. Figure 4 shows the geometry of the generic high aspect ratio UAV used in this work, and Table 1 lists its properties. More detailed information on the geometry can be found in [22, 49]. The wing structure consists of a hollow tubular spar, which is located at 45% of the chord. The spar diameter is determined by the local chord. The spar thickness varies linearly from the root value of 0.1 m to the tip thickness of 0.01 m. The cruise speed of the aircraft is set to 70 m/s. The longitudinal GLA is the focus of this study. Therefore, the state-space model consists of the horizontal velocity u , the vertical velocity w , the pitch rate q , the pitch angle θ , and the first thirty structural modal deformations and their rates. The right and left ailerons are deflected equally.

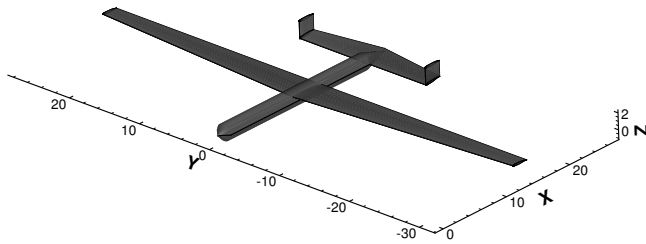


Figure 4. 3D geometry of generic UAV with large aspect ratio

Table 1. Aircraft geometric properties

Property	Value
Fuselage length	26.4 m
Wing span	58.6 m
Wing area	196 m ²
Wing taper	0.48
HT span	18 m
HT area	53.5 m ²
HT taper	0.7
VT span	4 m
VT area	8.9 m ²
VT taper	0.81

A. Model Comparison

Our unified dynamics framework allows for integrated design and control because it reveals strong inertial interactions, which are especially critical for very flexible aircraft. To illustrate this point, we give a frequency analysis by comparing the frequency characteristics of three models: 1) a statically deformed aircraft model (deformed model); 2) the statically deformed aircraft model augmented by a series of elastic modes (augmented model); and 3) the fully developed model under a unified framework (unified model).

Figure 5 shows the Bode diagrams that represent the transfer functions relating the vertical gust excitation to the load factor. The short period dynamics of the statically deformed aircraft is captured by two stable real poles at 8.9222 rad/s and 17.1779 rad/s. Figure 5 shows that: 1) The statically deformed model and the simplified model have similar DC-gain values whereas the DC-gain value of the proposed model is considerably lower. 2) The first dominant dynamics at 6.1 rad/s is dominated by the first structural mode that has a natural frequency of 4.849 rad/s; this dynamics is not captured by the statically deformed model. 3) At higher frequencies, the gain and the phase diagram for the

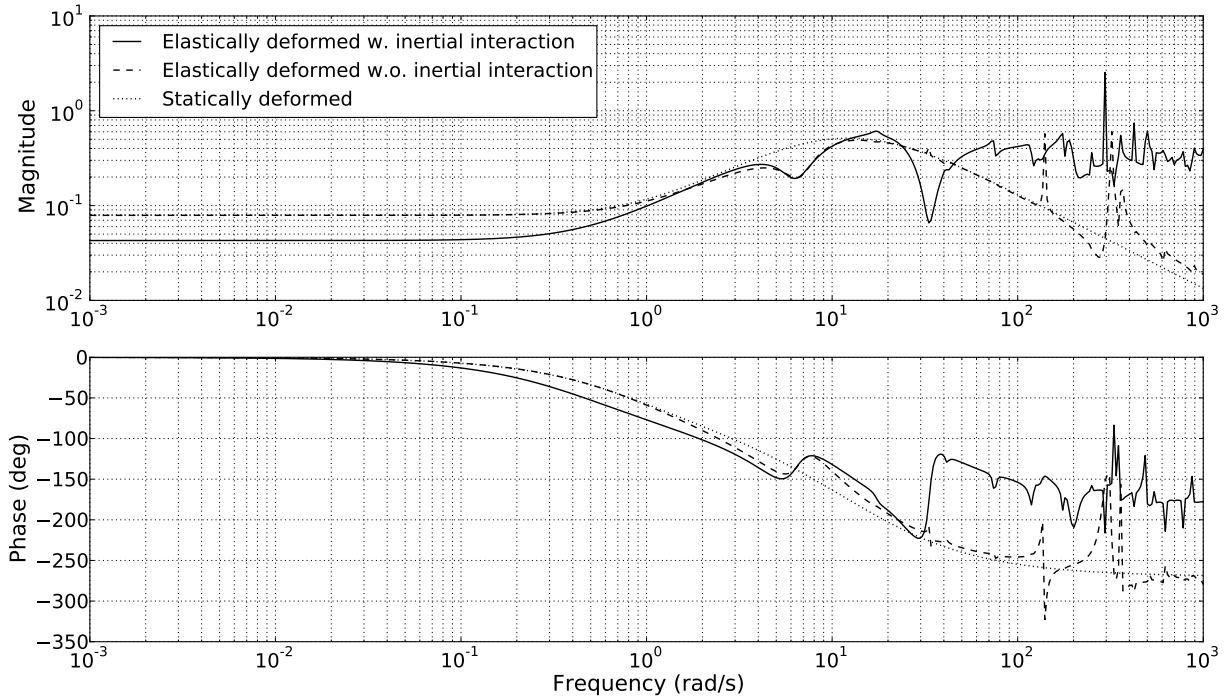


Figure 5. Bode diagrams for three aircraft models

augmented model show similar behavior to the rigid-body dynamics captured by the statically deformed model. The two spikes at 139.44 rad/s and 320.49 rad/s correspond to two modes that are heavily dominated by the first and second torsional dynamics. Because of the aerodynamic interaction, the torsional modes can significantly affect the rigid-body dynamics even when the inertial interaction is not considered. In contrast, the unified model is significantly different from the other two models, and at frequencies higher than the short period frequency, the transfer function gain is not attenuated. The Bode diagram clearly demonstrates that the exclusion of the inertial interaction makes a significant difference to the model accuracy at both low and high frequencies. Therefore, for the successful control of a very flexible aircraft the control design should be based on Eq. (15) that captures both the inertial and aerodynamic interactions.

B. Simulation Results

Table 2 lists the controller parameters used in the numerical analysis. The performance of MPC depends on the weighting matrices and the length of the control and prediction horizons. In this work the control and prediction horizons have the same length. The control horizon is selected through a trial-and-error process. The longer the control horizon, the better the results, but a very long horizon slows down the control signal calculation. The weighting

Table 2. Controller settings

Parameter	Symbol	Value
Sampling time	Δt	$2.5e-4$ s
Control horizon	N_u	20
Prediction horizon	N_p	20
Max surface deflection	$\max(\delta_e)$ or $\max(\delta_a)$	10 deg
Min surface deflection	$\min(\delta_e)$ or $\min(\delta_a)$	-10 deg
Max surface deflection rate	$\max(\Delta\delta_e/\Delta t)$ or $\max(\Delta\delta_a/\Delta t)$	60 deg/s

matrices can be chosen using performance optimization. The focus of this work is to use the proposed MPC framework to perform GLA and to compare its performance to a traditional MPC and an LQR controller. Therefore, we find the weighting matrices by trial and error. To find appropriate matrices, we first choose the R matrix. The R matrix is

diag [10 10]. The Q matrix is diagonal. We first choose the diagonal entries corresponding to rigid-body dynamics and then select the structural weightings. We use the following structure for the Q matrix:

$$Q = \text{diag} \begin{bmatrix} q_u & q_w & q_q & \underbrace{q_{\xi} \cdots q_{\xi}}_n & \underbrace{q_{\dot{\xi}} \cdots q_{\dot{\xi}}}_n & q_{\theta} \end{bmatrix} \quad (33)$$

where n is the number of structural modes used to construct the plant model.

Figures 6–14 show the results of a linear simulation with discrete gust excitations and gust lengths of 1 s, 0.5 s and 0.25 s. The results compare the rigid-body regulation and the GLA performance of our MPC, a traditional MPC, and an LQR control. The simulation results for a case without a GLA system are given as a reference. The maximum gust-induced stress levels at the wing root and mid-span locations are significantly reduced by the application of GLA. Moreover, GLA significantly reduces the maximum deviation of the rigid-body parameters from their steady-state values.

Table 3 gives the reduction percentage for the maximum gust-induced stress using the three controllers. Our MPC outperforms the traditional MPC and the LQR controller in terms of reducing the induced stress. When the aircraft is flying through a wide gust ($L_g=1$ s), all three controllers offer similar stress reduction capabilities. The rigid-body regulation performance of our MPC controller, shown in Fig. 6, is also comparable to that of the other controllers for a wide gust with $L_g=1$ s. As the gust becomes sharper, the GLA performance is reduced. While the performance of our controller is reduced by only 2.5%, that of the traditional MPC and LQR controllers is significantly reduced. This performance degradation can also be seen when we compare the rigid-body time-history of the three controllers (Figs. 10 and 13).

Table 3. Stress-level reduction for different controllers

L_g (s)	1.0	0.5	0.25
MPC with PE	45.4%	43.9%	42.9%
MPC	41.6%	37.7%	29.3%
LQR	44.5%	37.9%	26.7%

Table 4 shows the results when the controllers are applied to the aircraft while it flies through continuous gusts generated using the Dryden gust filter. We use the gust filter to generate ten gust profiles, each 10 s long. The stochastic simulation is first performed without GLA. The three controllers are then used to stabilize the aircraft and perform load alleviation. Table 4 presents the average RMS values and the average peak values of the gust-induced parameters such as load factor and maximum stress for the ten cases. Fig. 15 shows the time response of the three controllers to the applied stochastic excitations. In contrast to the discrete gust study, the traditional MPC and LQR controllers do not offer any improvement over the no-GLA case. Surprisingly, the exclusion of GLA resulted in lower average RMS and average peak values for both the rigid-body parameters and the stress levels. However, when the GLA system is excluded, the average RMS and peak values for the elevator deflection are considerably higher than those for the traditional MPC and LQR controllers. This makes the aircraft prone to control saturation when more severe gusts are considered.

The results for our MPC with PE have significantly lower RMS and peak values for both the rigid-body and structural parameters. The average RMS value of the load factor is reduced by 5.2% compared to the no-GLA results, and the average peak value of the load factor is reduced by 9.5%. The greatest improvement can be seen in the stress-level reduction: the average RMS value of the root maximum stress is reduced by 45.4% and the average peak value by 52.1%. Moreover, the average RMS and peak values for the elevator deflection are reduced.

When a system is inherently unstable, inaccuracies in the control effectiveness matrix (B) or the loss of control surface effectiveness can adversely affect the closed-loop performance. We consider the inaccuracies of the control surface effectiveness for both ailerons and elevators. The three controllers are applied to the same aircraft with 50% loss of control surface effectiveness. The simulation results for the crippled aircraft flying through two discrete gust excitations, $L_g=0.25$ and $L_g=0.5$, are presented in Figs. 17–22. Note that in the absence of GLA the aircraft experienced control surface saturation, and the controller failed to stabilize the plant when it was flying through a discrete gust with $L_g=0.5$. The traditional MPC and LQR controllers both suffered from the loss of control surface effectiveness. When the aircraft is flying through a sharp discrete gust ($L_g = 0.25$ s) the maximum stresses at both root and tip have high-frequency oscillations that can cause premature structural fatigue. The rigid-body tracking performance of these controllers is also degraded. In contrast, our MPC controlled the damaged aircraft effectively without experiencing high-frequency oscillations. The modified predictive controller damped out the excitation, but other controllers failed

Table 4. Average RMS and peak values of rigid-body and structural parameters in response to Dryden gust

		Load factor	w (m/s)	σ_{root} (MPa)	σ_{mid} (MPa)	δ_e (deg)	δ_a (deg)
Average RMS	MPC with PE	0.4162	1.2222	2.5867e+06	2.3782e+05	2.00002	0.5254
	MPC	0.5724	2.3311	5.0891e+06	4.5781e+05	1.2768	0.9227
	LQR	0.5658	2.2951	4.9946e+06	4.5038e+05	1.2852	0.9128
	No GLA	0.4394	1.6595	4.7404e+06	4.4014e+05	2.6167	–
Average peak	MPC with PE	1.0426	2.3748	5.1686e+06	5.1574e+05	4.3849	1.36003
	MPC	1.5687	4.5455	1.0166e+07	1.0208e+06	2.9316	2.3634
	LQR	1.5317	4.4586	9.9287e+06	9.9498e+05	2.9467	2.3456
	No GLA	1.1521	3.1054	1.0802e+07	1.0826e+06	5.9604	–

to reject the excitation during the simulation.

We also consider stochastic continuous gusts to analyze the controller performance in the presence of control ef-

Table 5. Average RMS and peak values of rigid-body and structural parameters in response to Dryden gust

		Load factor	w (m/s)	σ_{root} (MPa)	σ_{mid} (MPa)	δ_e (deg)	δ_a (deg)
Average RMS	MPC with PE	0.7128	2.0928	4.9537e+06	4.3503e+05	3.4353	1.4580
	LQR	0.9821	3.7354	8.9246e+06	7.4617e+05	2.5772	3.3027
Average peak	MPC with PE	1.9363	4.2413	1.0473e+07	9.8308e+05	7.6642	3.6368
	LQR	2.6036	7.9605	2.0225e+07	1.7985e+06	6.1842	7.6825

fectiveness inaccuracies. Table 5 presents these results. In the no-GLA case and when a traditional MPC was used, control input saturation destabilized the system. On the other hand, our MPC method and the LQR controller successfully stabilized the aircraft. Figure 16 shows the responses of these two controllers to the excitations. The results in Table 5 show that the average RMS and peak values corresponding to our MPC are significantly lower than those for the LQR.

VII. Conclusions

In this work, the nonlinear equations of motion of a highly flexible aircraft were derived. A three-dimensional panel-code was developed and modified to obtain the aerodynamic responses to pulse excitations. These were used to construct a linearized state-space representation of the unsteady aerodynamics. A model-predictive controller was developed to perform gust load alleviation for an aircraft encountering discrete and continuous atmospheric disturbances. To improve the performance and robustness of the traditional model-predictive formulation, a feedback loop was introduced to improve the prediction performance of the controller. The predictive framework was applied to a highly flexible aircraft to demonstrate the load alleviation effectiveness of the controller. The feedback loop improved the controller performance in terms of the rigid-body dynamics while maintaining the same level of structural relaxation for different gust scales. It also made the controller less sensitive to the loss of control surface effectiveness. The proposed predictive controller performed better than a linear quadratic controller at regulating the maximum stress and the rigid-body parameters. The proposed framework integrates aerostructural design with active control, which fully exploits the potential of an active aeroservoelastic wing, making it possible to consider a higher aspect ratio and more flexible structures when designing aircraft.

Acknowledgments

The authors would like to thank the Natural Sciences and Engineering Research Council of Canada (NSERC) for providing financial support.

References

- [1] Suzuki, S., “Simultaneous Structure/Control Design Synthesis for Aero-Servo-Elastic System,” *Finite Elements in Analysis and Design*, Vol. 14, No. 2–3, October 1993, pp. 197–208.

- [2] Moulin, B. and Karpel, M., "Gust Loads Alleviation Using Special Control Surfaces," *Journal of Aircraft*, Vol. 44, No. 1, 2007, pp. 17–25.
- [3] Woods-Vedeler, J. and Pototzky, A., "Rolling Maneuver Load Alleviation Using Active Controls," *Journal of Aircraft*, Vol. 32, No. 1, 1995, pp. 68–76.
- [4] Gaulocher, S., Roos, C., and Cumer, C., "Aircraft Load Alleviation During Maneuvers Using Optimal Control Surface Combinations," *Journal of Guidance, Control, and Dynamics*, Vol. 30, No. 2, 2007, pp. 591–600.
- [5] Pendleton, E., Bessette, D., Field, P., Miller, G., and Griffin, K., "Active Aeroelastic Wing Flight Research Program: Technical Program and Model Analytical Development," *Journal of Aircraft*, Vol. 37, No. 4, 2000, pp. 554–561.
- [6] Zink, S., Raveh, D., and Mavris, D., "Integrated Trim and Structural Design Process for Active Aeroelastic Wing Technology," *Journal of Aircraft*, Vol. 40, No. 3, 2003, pp. 523–531.
- [7] Abel, I. and Newsom, J. R., "Langley Research Center Contributions in Advancing Active Control Technology," Tech. Rep. 81N19002, NASA Langley Research Center, 1981.
- [8] Karpel, M., "Design for Active Flutter Suppression and Gust Alleviation Using State-Space Aeroelastic Modeling," *Journal of Aircraft*, Vol. 19, No. 3, March 1982, pp. 221–227.
- [9] Ostrower, J., "FAA and Boeing Agree on 747-8 OAMS Special Condition," [online], March 2011, Air Transport Intelligence, <http://www.flightglobal.com/articles/2011/03/23/354600/faa-and-boeing-agree-on-747-8-oams-special-condition.html>.
- [10] Noll, T. E., Ishmael, S. D., Henwood, B., Perez-Davis, M. E., Tiffany, G. C., Madura, J., Gaier, M., Brown, J. M., and Wierzbanski, T., "Technical Findings, Lessons Learned, and Recommendations Resulting from the Helios Prototype Vehicle Mishap," Tech. Rep. 20070022260, NASA, 2007.
- [11] McLean, D. and Prasad, R. A., "A Structural Load Alleviation Control System for a Large Aircraft," *Transactions of the Institute of Measurement and Control*, Vol. 2, No. 1, Jan.-Mar. 1980, pp. 25–37.
- [12] Aouf, N., Boulet, B., and Botez, R., " H_2 and H_∞ Optimal Gust Load Alleviation for a Flexible Aircraft," *Proceedings of American Control Conference*, Chicago, IL, June 2000.
- [13] Silva, W. A., Vartio, E., Shimko, A., Kvaternik, R. G., Eure, K. W., and Scott, R. C., "Development of Aeroservoelastic Analytical Models and Gust Load Alleviation Control Laws of a SensorCraft Wind-Tunnel Model Using Measured Data," *47th AIAA/ASME/ASCE/AHS/ASC Structures, Structural Dynamics, and Materials Conference*, No. AIAA 2006–1935, Newport, RI, May 2006.
- [14] Zeng, J., Moulin, B., de Callafon, R., and Brenner, M. J., "Adaptive Feedforward Control for Gust Load Alleviation," *Journal of Guidance, Control, and Dynamics*, Vol. 33, No. 3, May-June 2010, pp. 862–872.
- [15] Wildschek, A. and Maier, R., "Integrated Adaptive Feed-Forward Control of Atmospheric Turbulence Excited Rigid Body Motions and Structural Vibrations on a Large Transport Aircraft," *American Control Conference*, Seattle, WA, June 2008.
- [16] Wildschek, A., Maier, R., Hromcik, M., Hanis, T., Schirrer, A., Kozek, M., Westermayer, C., and Hemedi, M., "Hybrid Controller for Gust Load Alleviation and Ride Comfort Improvement Using Direct Lift Control Flaps," *3rd European Conference for Aerospace Sciences (EUCASS)*, 2009.
- [17] Dillsaver, M. J., Cesnik, C. E. S., and Kolmanovsky, I. V., "Gust Load Alleviation Control for Very Flexible Aircraft," *AIAA Atmospheric Flight Mechanics Conference*, No. AIAA 2011–6368, Portland, OR, 2011.
- [18] Cesnik, C. E. S., Senatore, P. J., Su, W., Atkins, E. M., Shearer, C. M., and Pitcher, N. A., "X-Hale: A Very Flexible UAV for Nonlinear Aeroelastic Tests," *51st AIAA Structures, Structural Dynamics, and Materials Conference*, Orlando, FL, April 2010.
- [19] Schmidt, D. K. and Raney, D. L., "Modeling and Simulation of Flexible Flight Vehicles," *Journal of Guidance, Control, and Dynamics*, Vol. 24, No. 3, 2001, pp. 539–546.
- [20] Meirovitch, L. and Tuzcu, I., "Integrated Approach to the Dynamics and Control of Maneuvering Flexible Aircraft," Tech. Rep. CR-2003-211748, NASA, June 2003.
- [21] Patil, M. J. and Hodges, D. H., "Flight Dynamics of Highly Flexible Flying Wings," *Journal of Aircraft*, Vol. 43, No. 3, 2006, pp. 1790–1798.
- [22] Shearer, C. M. and Cesnik, C. E., "Nonlinear Flight Dynamics of Very Flexible Aircraft," *Journal of Aircraft*, Vol. 44, No. 5, Sep.-Oct. 2007, pp. 1528–1545.
- [23] Baluch, H. A. and van Tooren, M., "Modified Inertially Coupled Equations of Motion for Flexible Aircraft with Coupled Vibrations," *Journal of Aircraft*, Vol. 46, No. 1, 2009, pp. 107–115.
- [24] Tuzcu, I. and Nguyen, N., "Aeroelastic Modeling and Adaptive Control of GTM," *Proceedings of the AIAA Atmospheric Flight Mechanics Conference*, No. AIAA2010–7503, Toronto, Canada, August 2010.
- [25] Haghighat, S., Martins, J. R. R. A., and Liu, H. H. T., "Aeroservoelastic Design Optimization of a Flexible Wing," *Journal of Aircraft*, Vol. 49, No. 2, Mar.-Apr. 2012.

- [26] Karpel, M., "Procedures and Models for Aeroservoelastic Analysis and Design," *Journal of Applied Mathematics and Mechanics (ZAMM)*, Vol. 81, No. 9, 2001, pp. 579–592.
- [27] Crisfield, M. A., "A Consistent Co-Rotational Formulation for Non-Linear, Three-Dimensional, Beam-Elements," *Computer Methods in Applied Mechanics and Engineering*, Vol. 81, No. 2, 1990, pp. 131–150.
- [28] Crisfield, M. A., Galvanetto, U., and Jelenic, G., "Dynamics of 3-D Co-Rotational Beams," *Computational Mechanics*, Vol. 20, No. 6, 1997, pp. 507–519.
- [29] Li, Z. X., "A Co-Rotational Formulation for 3D Beam Element Using Vectorial Rotational Variables," *Computational Mechanics*, Vol. 39, No. 3, 2007, pp. 309–322.
- [30] Silva, W. A., "Application of Nonlinear Systems Theory to Transonic Unsteady Aerodynamic Responses," *Journal of Aircraft*, Vol. 30, No. 5, Sept.-Oct. 1993, pp. 660–668.
- [31] Silva, W. A., *Discrete-Time Linear and Nonlinear Aerodynamic Impulse Responses for Efficient CFD Analysis*, Ph.D. thesis, College of William and Mary in Virginia, 1997.
- [32] Raveh, D. E. and Mavris, D. N., "Reduced-Order Models Based on CFD Impulse and Step Responses," *42nd AIAA/ASME/ASCE/AHS/ASC Structures, Structural Dynamics, and Materials Conference*, Seattle, WA, April 2001, AIAA 2001–1527.
- [33] Silva, W. A. and Bartels, R. E., "Development of Reduced-Order Models for Aeroelastic Analysis and Flutter Prediction Using the CFL3Dv6.0 Code," *Journal of Fluids and Structures*, Vol. 19, No. 6, July 2004, pp. 729–745.
- [34] Lucia, D. J., Beran, P. S., and Silva, W. A., "Reduced-Order Modeling: New Approaches for Computational Physics," *Progress in Aerospace Sciences*, Vol. 40, No. 1–2, February 2004, pp. 51–117.
- [35] Juang, J. and Pappa, R. S., "An Eigensystem Realization Algorithm for Modal Parameter Identification and Model Reduction," *Journal of Guidance, Control, and Dynamics*, Vol. 8, No. 5, 1985, pp. 620–627.
- [36] Haghighat, S., Liu, H. H. T., and Martins, J. R. R. A., "Application of Model Predictive Control to Gust Loads Alleviation Systems," *AIAA Atmospheric Flight Mechanics*, No. AIAA 2009–5929, Chicago, IL, 2009.
- [37] Zole, A. and Karpel, M., "Continuous Gust Response and Sensitivity Derivatives Using State-Space Models," *Journal of Aircraft*, Vol. 31, No. 5, 1994, pp. 1212–1214.
- [38] Kwon, W. and Han, S., *Receding Horizon Control: Model Predictive Control for State Models*, Springer, 2005.
- [39] Abate, A. and Ghaoui, L. E., "Robust Model Predictive Control Through Adjustable Variables: An Application to Path Planning," *43rd IEEE Conference on Decision and Control*, Berkeley, CA, December 2004.
- [40] Richards, A. and How, J. P., "Robust Variable Horizon Model Predictive Control for Vehicle Maneuvering," *International Journal of Robust and Nonlinear Control*, Vol. 16, No. 7, May 2006, pp. 333–351.
- [41] Mayne, D. Q., Rawlings, J. B., Rao, C. V., and Sokaert, P. O. M., "Constrained Model Predictive Control: Stability and Optimality," *Automatica*, Vol. 36, No. 6, June 2000, pp. 789–814.
- [42] Boyd, S. and Vandenberghe, L., *Convex Optimization*, Cambridge University Press, 2004.
- [43] Bryson, A. E. and Ho, Y. C., *Applied Optimal Control: Optimization, Estimation, and Control*, Blaisdell Publishing, 1969.
- [44] Batina, I., *Model Predictive Control for Stochastic Systems by Randomized Algorithms*, Ph.D. thesis, Technische Universiteit Eindhoven, 2004.
- [45] Richards, A. and How, J. P., "Analytical Performance Prediction for Robust Constrained Model Predictive Control," *AIAA Guidance, Navigation, and Control Conference*, No. AIAA 2004–5110, Providence, RI, 2004.
- [46] Richards, A. and How, J. P., "Robust Model Predictive Control with Imperfect Information," *American Control Conference*, Portland, OR, 2005.
- [47] Garcia-Gabin, W., Zambrano, D., and Camacho, E. F., "Multivariable Model Predictive Control of Processes with Unstable Transmission Zeros," *Proceedings of the American Control Conference*, Anchorage, AK, 2002, pp. 4189–4190.
- [48] Garcia-Gabin, W. and Camacho, E. F., "MPC Tuning for Systems with Right Half Plane Zeros," *WSEAS Transactions on Circuits and Systems*, Vol. 3, No. 1, 2004, pp. 794–799.
- [49] Shearer, C. M. and Cesnik, C. E. S., "Trajectory Control for Very Flexible Aircraft," *Journal of Guidance, Control, and Dynamics*, Vol. 31, No. 2, 2008, pp. 340–357.

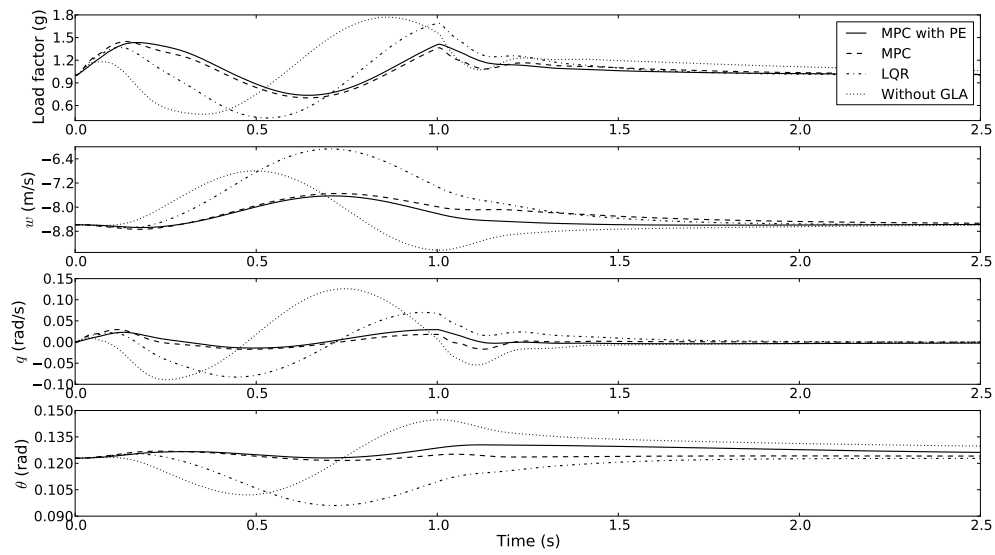


Figure 6. Load factor and rigid-body parameters ($L_g = 1.0$ s)

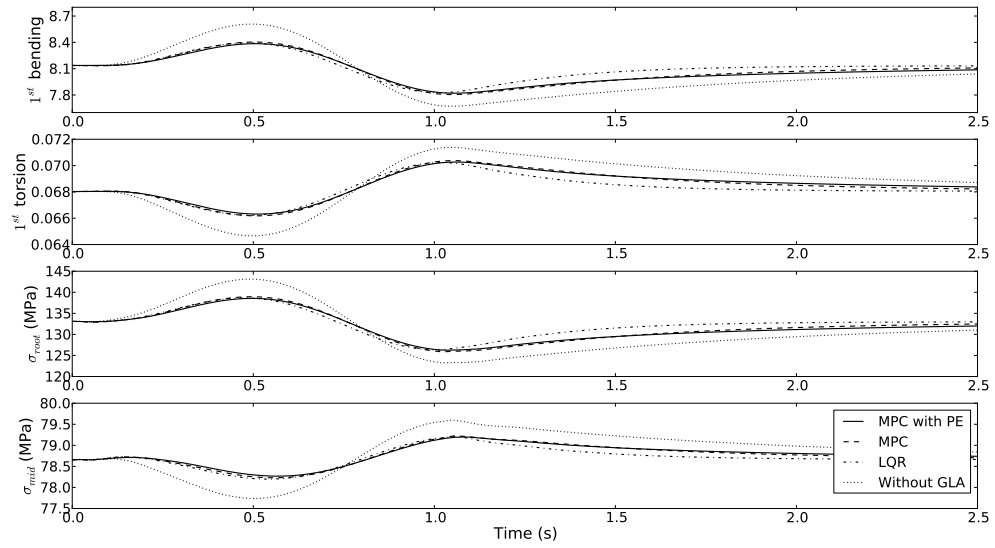


Figure 7. Structural modes and wing root and mid stresses ($L_g = 1.0$ s)

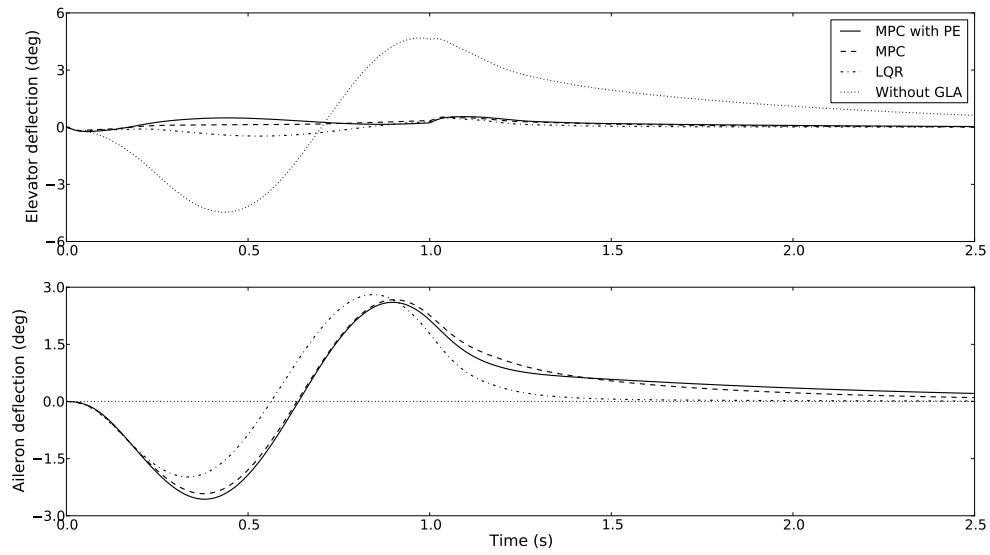


Figure 8. Control surface deflections ($L_g = 1.0$ s)

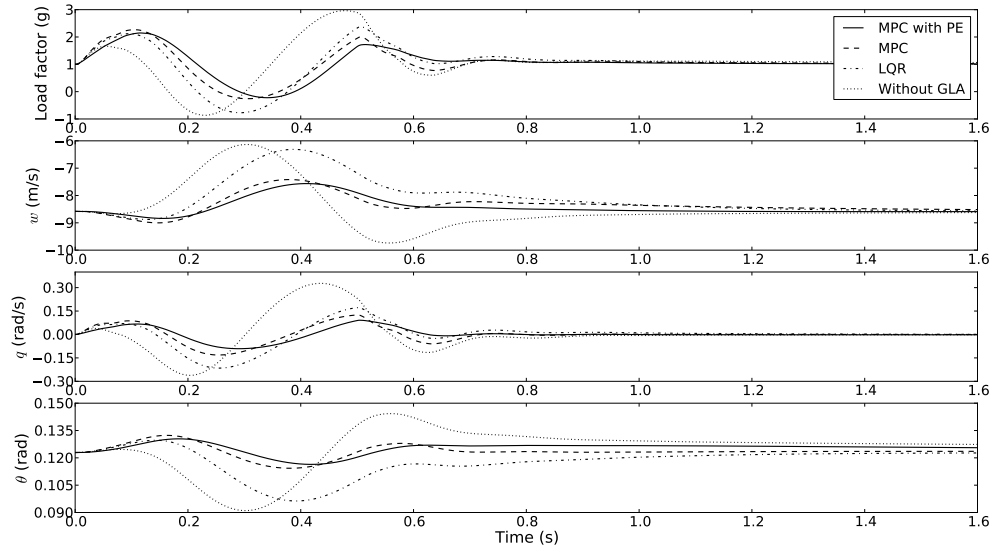


Figure 9. Load factor and rigid-body parameters ($L_g = 0.5$ s)

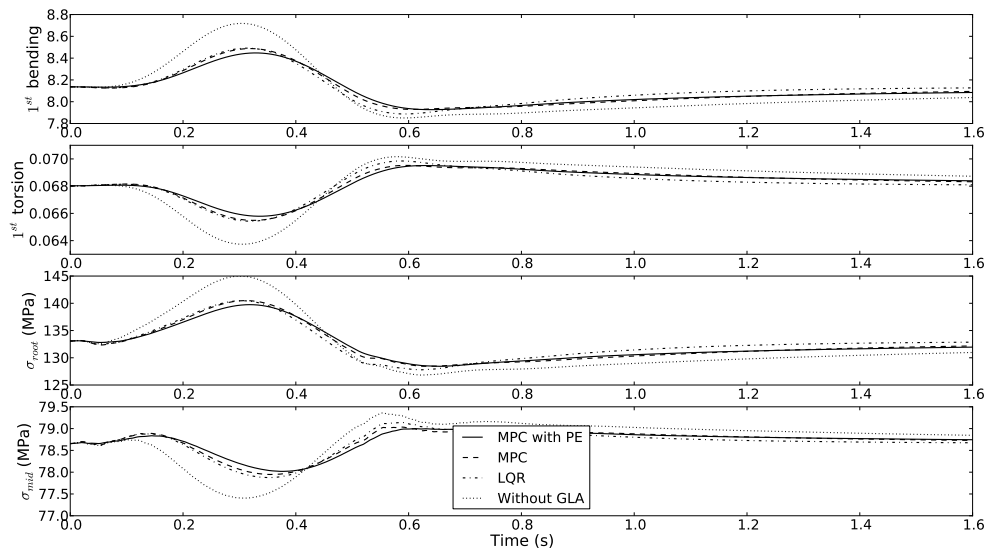


Figure 10. Structural modes and wing root and mid stresses ($L_g = 0.5$ s)

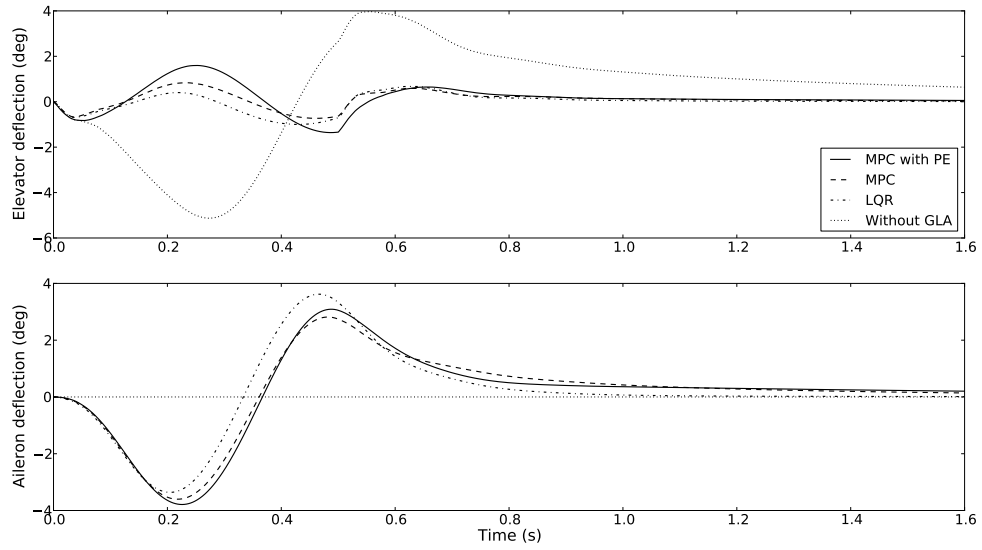


Figure 11. Control surface deflections ($L_g = 0.5$ s)

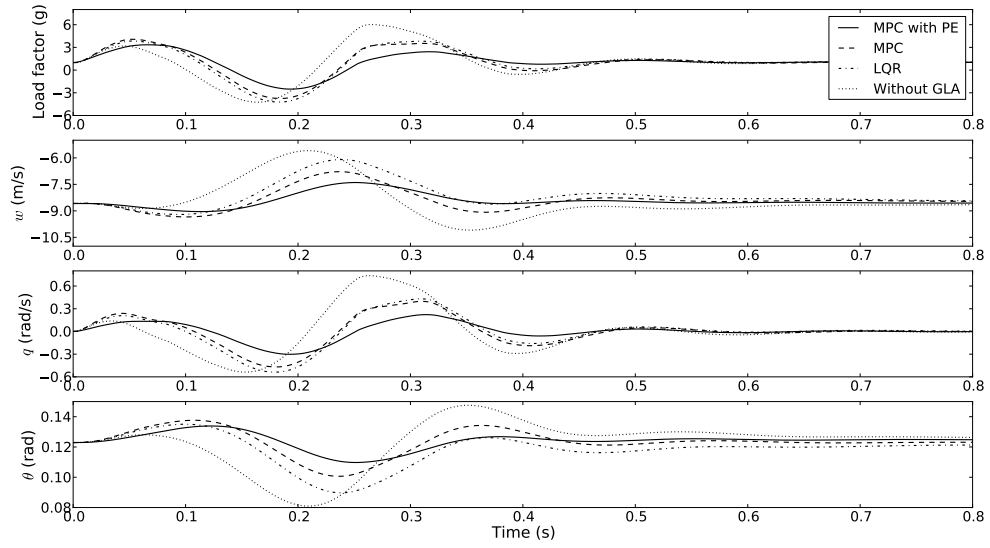


Figure 12. Load factor and rigid-body parameters ($L_g = 0.25$ s)

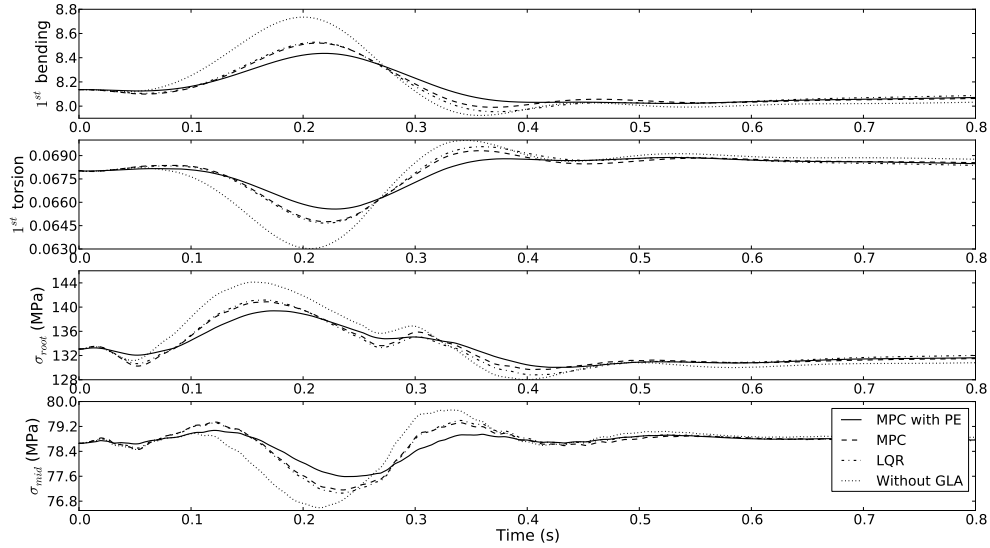


Figure 13. Structural modes and wing root and mid stresses ($L_g = 0.25$ s)

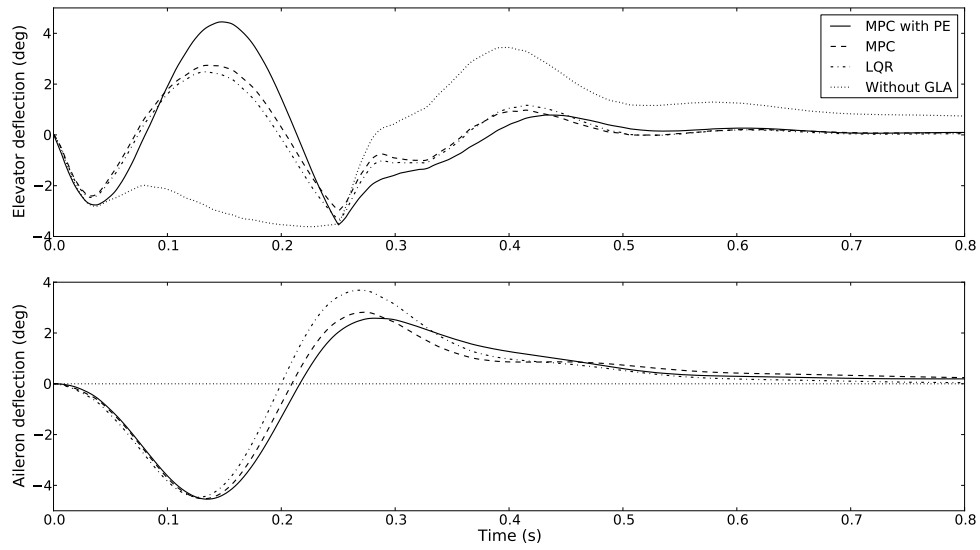


Figure 14. Control surface deflections ($L_g = 0.25$ s)

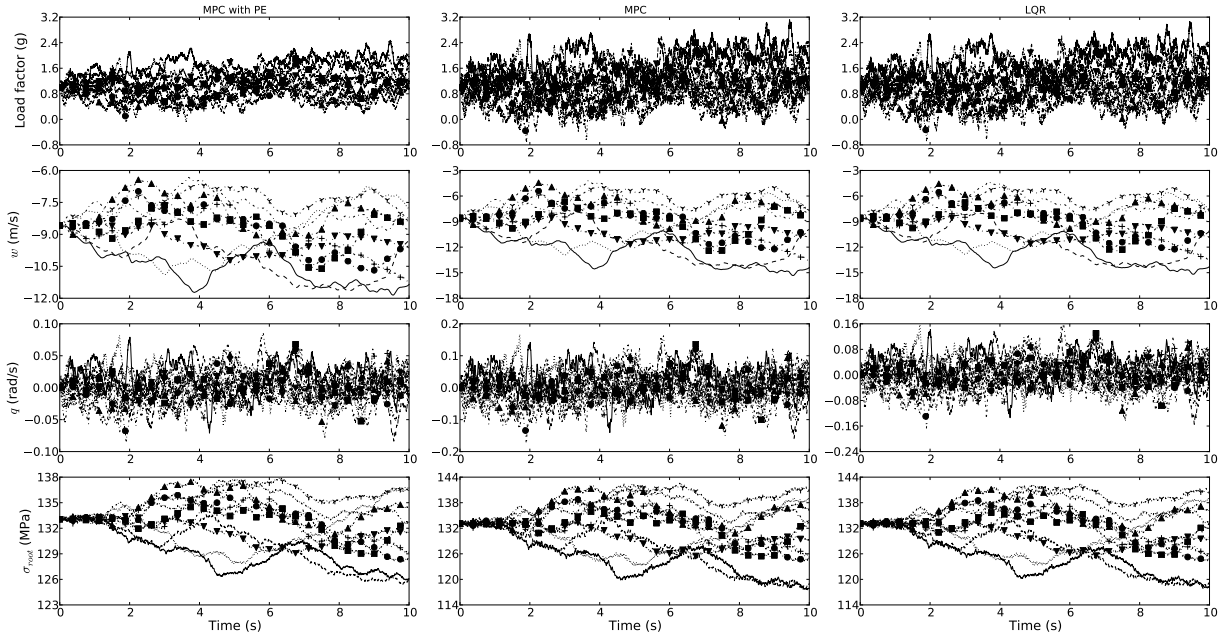


Figure 15. Response of aircraft GLA system to continuous stochastic gusts

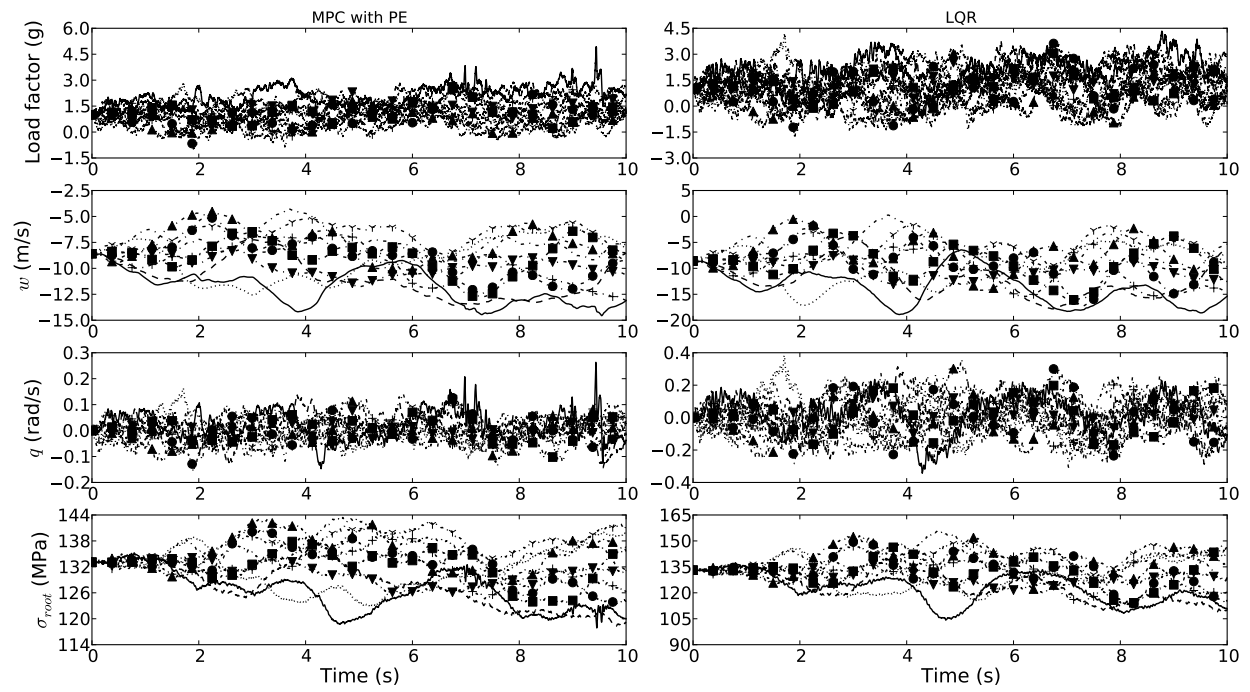


Figure 16. Response of crippled-aircraft GLA system to continuous stochastic gusts

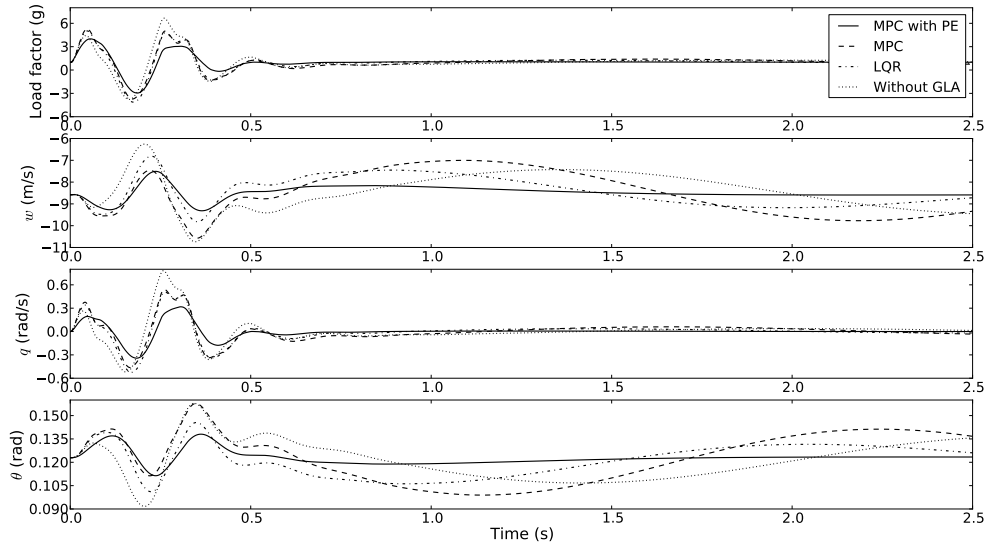


Figure 17. Load factor and rigid-body parameters for crippled aircraft ($L_g = 0.25$ s)

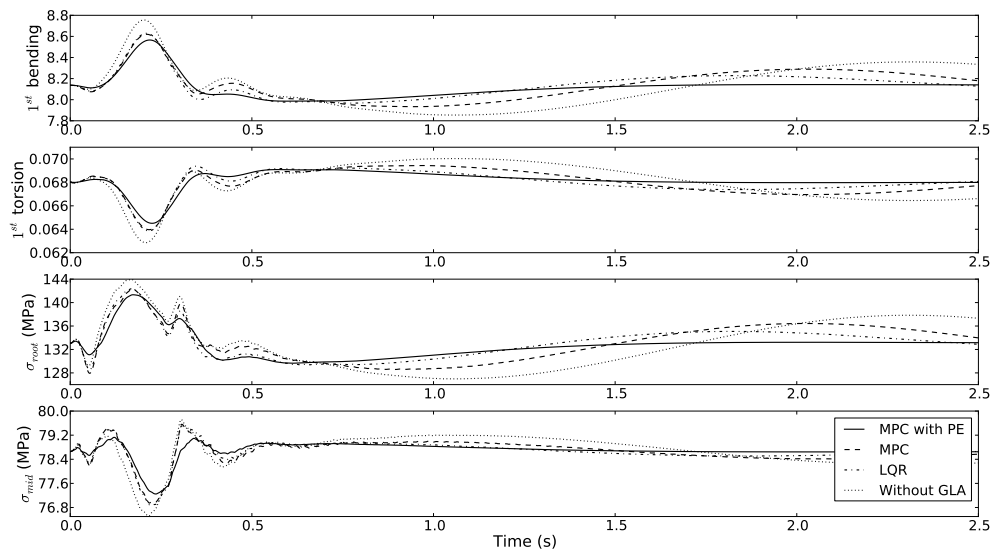


Figure 18. Structural modes and wing root and mid stresses for crippled aircraft ($L_g = 0.25$ s)

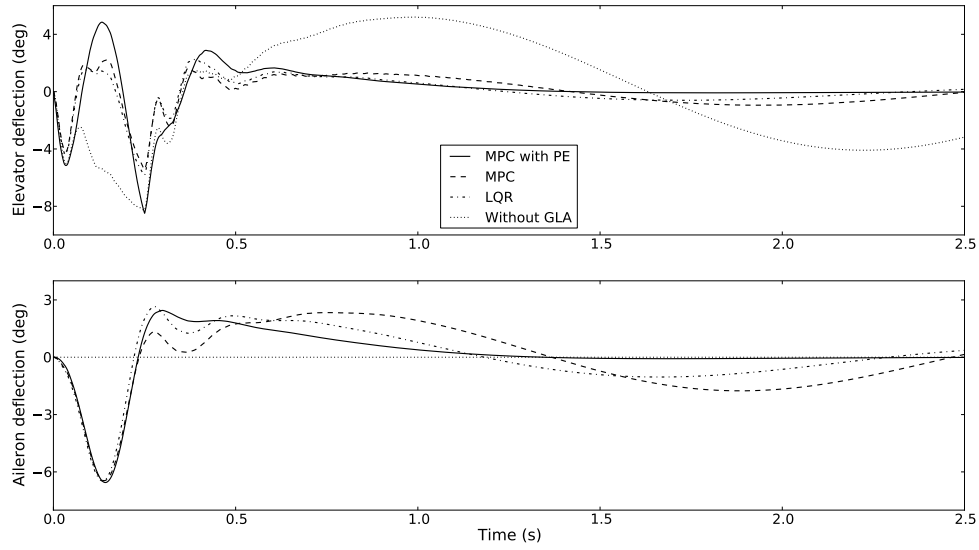


Figure 19. Control surface deflections for crippled aircraft ($L_g = 0.25$ s)

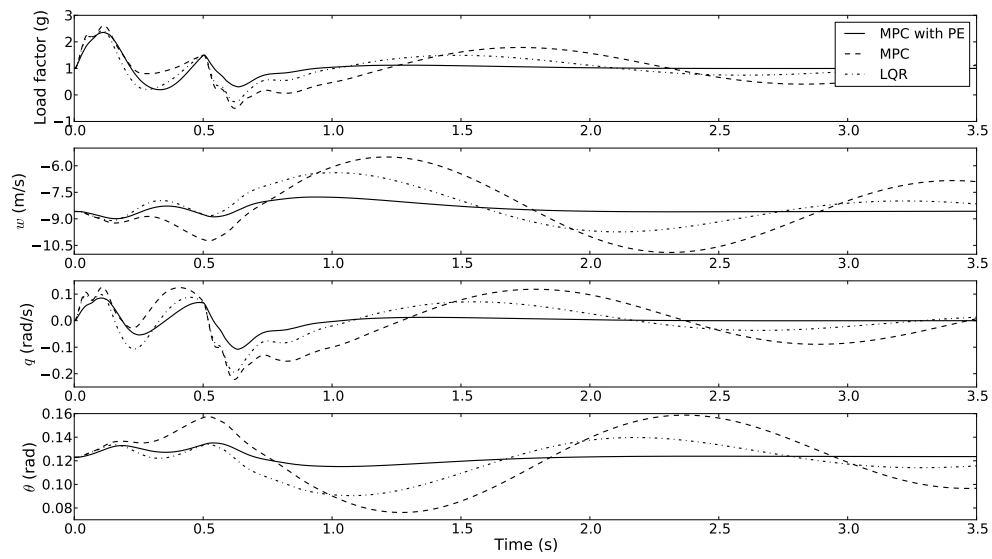


Figure 20. Load factor and rigid-body parameters for crippled aircraft ($L_g = 0.5$ s)

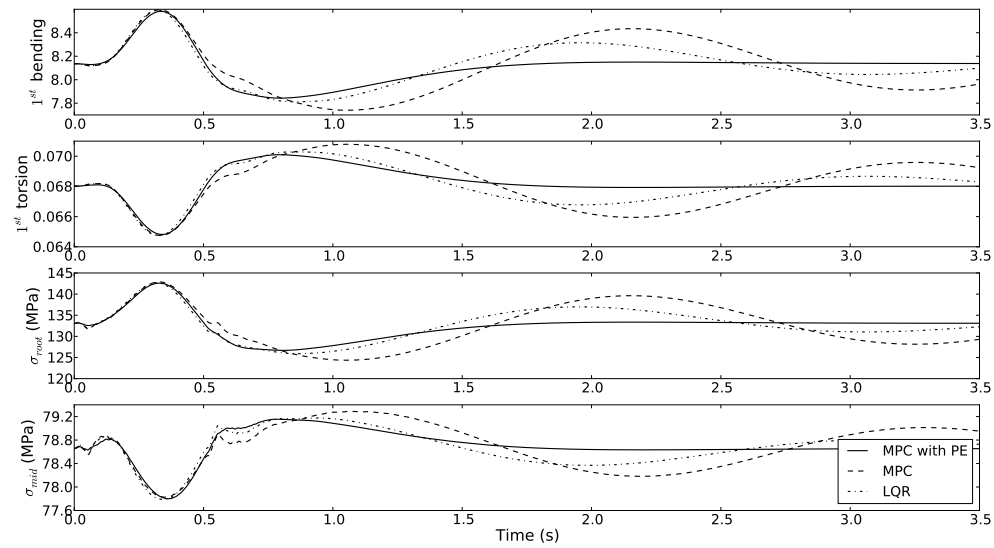


Figure 21. Structural modes and wing root and mid stresses for crippled aircraft ($L_g = 0.5$ s)

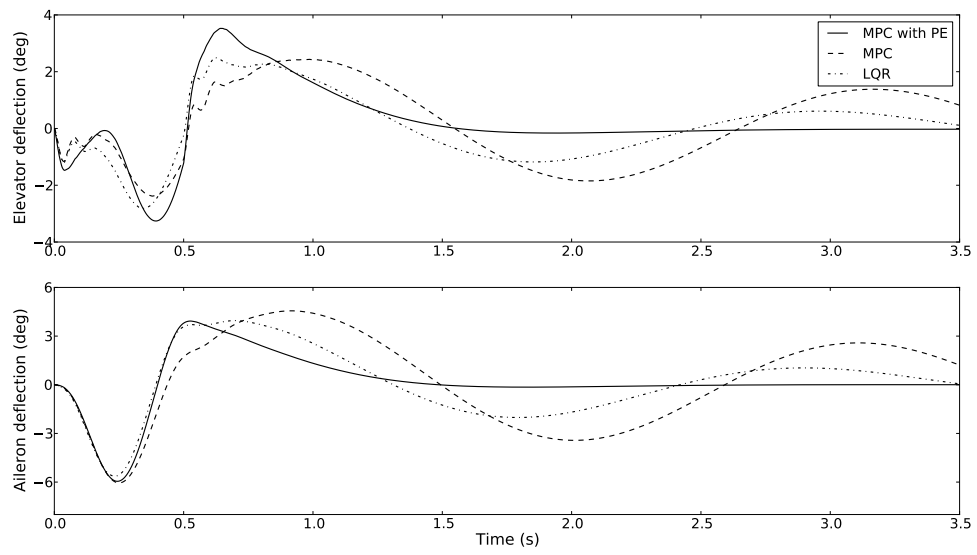


Figure 22. Control surface deflections for crippled aircraft ($L_g = 0.5$ s)